NMR IN BIOMEDICINE
NMR Biomed. 2007; **20**: 591–601
Published online 8 January 2007 in Wiley InterScience
(www.interscience.wiley.com) DOI:10.1002/nbm.1126

Improved cine displacement-encoded MRI using balanced steady-state free precession and time-adaptive sensitivity encoding parallel imaging at 3 T

Daniel Kim[1]* and Peter Kellman[2]

[1]Department of Radiology, New York University, New York, NY 10016, USA
[2]Laboratory of Cardiac Energetics, National Heart Lung and Blood Institute, National Institutes of Health, Bethesda, MD 20892, USA

Received 2 August 2006; Revised 28 September 2006; Accepted 31 October 2006

ABSTRACT: Cine displacement-encoded MRI is a promising modality for quantifying regional myocardial function. However, it has two major limitations: low signal-to-noise ratio (SNR) and data acquisition efficiency. The purpose of this study was to incrementally improve the SNR and the data acquisition efficiency of cine displacement-encoded MRI through the combined use of balanced steady-state free precession (b-SSFP) imaging, 3T imaging, echo-combination image reconstruction, and time-adaptive sensitivity encoding (TSENSE) parallel imaging. Phantom experiments were performed to empirically determine the optimal excitation angle (α) and to estimate the measurement errors in the presence of 130 Hz peak-to-peak static magnetic field (B_0) variation. The optimal α was determined to be 20°. The intrinsic phase correction in the echo-combination effectively reduced the phase error, which produced small displacement errors (0.11 versus 0.11 mm) and negligible strain errors (−0.001 versus −0.002). Six healthy volunteers were imaged in three short-axis levels of the heart to evaluate the SNR and the relative accuracy of strain calculations. Compared with the 24-heartbeat cine echo-planar imaging acquisition, the 24-heartbeat non-accelerated b-SSFP acquisition yielded approximately 65% higher SNR, and the 12-heartbeat twofold accelerated b-SSFP acquisition yielded approximately 28% higher SNR. The 12-heartbeat twofold accelerated b-SSFP acquisition yielded functional maps with spatial resolution of 3.6×3.6 mm, temporal resolution of 35 ms, and relatively high SNR (31.2 ± 5.4 at end diastole; 19.9 ± 3.6 at end systole; 10.3 ± 1.1 at late diastole; mean ± SD). The left ventricular strain values between the non-accelerated and twofold accelerated b-SSFP acquisitions correlated strongly (slope = 0.99; bias = 0.00; $R^2 = 0.91$) and were in excellent agreement. The combined implementation of b-SSFP imaging, 3T imaging, echo-combination image reconstruction, and TSENSE parallel imaging can be used to incrementally improve the cine displacement-encoded MRI pulse sequence. Copyright © 2007 John Wiley & Sons, Ltd.

KEYWORDS: MRI; SENSE; strain; TSENSE; function; displacement; tagging; SSFP

INTRODUCTION

Non-invasive assessment of regional myocardial function plays a critical role in the management of heart disease. The most widely used modalities for the assessment of regional wall motion are echocardiography and cine MRI. However, these qualitative modalities often yield results that require subjective interpretations which are reader dependent. Quantitative assessment of regional wall motion can be used to minimize the inter-observer and intra-observer variability. Currently available quantitative modalities for the assessment of regional cardiac function include tissue Doppler imaging (1), myocardial tagged MRI (2,3), velocity-encoded MRI (4–6), harmonic phase image (HARP) processing (7), and displacement-encoded MRI (8–10), with each modality having advantages and disadvantages.

In particular, cine displacement-encoded MRI is a promising modality for quantifying regional myocardial function, because it combines advantageous features of myocardial tagged MRI (Lagrangian strain) and velocity-encoded MRI (pixel-wise spatial resolution), as previously described (10). This modality has been validated against the well-established myocardial tagged MRI in a limited number of healthy volunteers (9,10). However, cine displacement-encoded MRI has two major limitations: (1) low signal-to-noise ratio (SNR) because of the 50% signal loss inherent to stimulated echoes; (2) low data acquisition efficiency because of a need to

**Correspondence to:* D. Kim, Department of Radiology, New York University, 650 1st Ave., 600-A New York, NY 10016, USA.
E-mail: dan.kim@med.nyu.edu
Contract/grant sponsor: Radiological Society of North America Research & Education Foundation; *contract/grant number:* SD0605.

Abbreviations used: b-SSFP, balanced steady-state free precession; SNR, signal-to-noise ratio; 1D, one-dimensional; 2D, two-dimensional; SENSE, sensitivity encoding for fast MRI; TSENSE, time-adaptive sensitivity encoding parallel acquisition; SPAMM, spatial modulation of magnetization; CSPAMM, complementary SPAMM; B_0, static magnetic field; B_1, radio-frequency field; ECG, electrocardiogram; RF, radio-frequency; EPI, echo-planar imaging; RMS, root-mean-square; FWHM, full width at half maximum; E_2, second principal strain.

acquire multiple data sets for two-dimensional (2D) motion encoding, phase correction, and suppression of artifact-generating echoes due to T_1 relaxation. Consequently, cine displacement-encoded MRI is typically acquired in relatively long breath-holds, which renders it impractical for clinical applications.

Existing methods to augment the SNR include echo-combination image reconstruction (9,11), balanced steady-state free precession (b-SSFP) imaging (12–18), and 3T imaging. Existing methods to increase the data acquisition rate include b-SSFP imaging, parallel imaging, such as sensitivity encoding for fast MRI (SENSE) (19,20) or time-adaptive sensitivity encoding (TSENSE) (21), and echo-combination image reconstruction (11), which can be used to eliminate the need to acquire extrinsic phase reference data. To date, these methods have not been jointly implemented for cine displacement-encoded MRI. The purpose of this study was to incrementally improve the cine displacement-encoded MRI pulse sequence by combining these strategies.

THEORY

In this section, we briefly describe the basic principles of the echo-combination reconstruction in order to clarify the technical issues relevant to this study.

Echo-combination reconstruction

In displacement-encoded MRI, as well as in HARP MRI, myocardial displacement is encoded on the phase of the magnetization using 1-1 spatial modulation of magnetization (SPAMM) (2) or complementary SPAMM (CSPAMM) pulses (9,10,22,23). The application of SPAMM or CSPAMM pulses generates two displacement-encoded echoes in k-space. The echo-combination reconstruction exploits the Fourier property of conjugate symmetry and combines the two displacement-encoded phase images as the phase difference divided by two, as previously described (9,11).

Figure 1 shows a sample k-space that illustrates the mechanism of intrinsic phase correction in the echo-combination reconstruction. Between the two displacement-encoded echoes, the phase due to displacement is identical in magnitude but opposite in polarity (9,11), whereas the phase error due to static magnetic field (B_0) inhomogeneity is different, although its difference is relatively small. The advantages of the echo-combination reconstruction over the conventional method include improved SNR, improved image acquisition efficiency by not acquiring the extrinsic phase reference data, and elimination of phase errors due to scan-to-scan physiological (e.g. motion) and imaging variations [e.g. radio-frequency (RF) field (B_1) phase variation] by performing intrinsic phase correction from the same

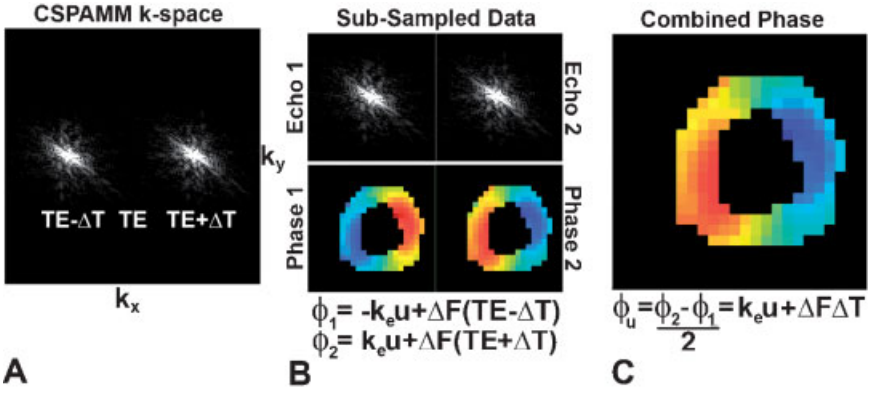

Figure 1. Echo combination reconstruction and its basic mathematical description. (A) In the echo-combination displacement-encoded MRI, the two echoes are positioned at $k_x = -0.25$ cycles/pixel and $k_x = 0.25$ cycles/pixel using the 1-1 CSPAMM pulses. (B) The CSPAMM k-space is divided into two 96×96 k-space matrices, and the two sub-sampled k-space data are separately reconstructed, as previously described (9). (C) The two sub-sampled phase images are combined as the phase difference divided by two. The phase difference eliminates phase error due to scan-to-scan physiological (e.g. motion) and imaging variations (e.g. B_1 phase variation) by performing intrinsic phase correction from the same data. However, the intrinsic phase correction does not eliminate the phase error due to B_0 inhomogeneity and susceptibility. The residual phase error is equal to $\Delta F \Delta T$, where ΔF is the off-resonant frequency, and ΔT is the time interval between each sub-sampled echo and *TE*. k_x, Spatial frequency in the frequency-encoding direction; u, displacement; ΔT, time interval between each sub-sampled echo and *TE*; ϕ, phase; ϕ_1, phase of echo 1; ϕ_2, phase of echo 2; ϕ_u, displacement-encoded phase with residual phase error.

DOI: 10.1002/nbm

data. A disadvantage of the echo-combination reconstruction compared with the conventional method is that the phase error due to B_0 inhomogeneity is not eliminated after the echo combination reconstruction (Fig.1). Specifically, the residual phase error is equal to $\Delta F \Delta T$, where ΔF is the off-resonant frequency and ΔT is the time interval between each echo and *TE* of the original CSPAMM k-space. The calculated errors in the phase and displacement are 0.27 radians and 0.29 mm, respectively, when using the image parameters described in this study ($\Delta T = 0.34$ ms) and assuming a worst case scenario of 130 Hz peak-to-peak B_0 variation in the heart at 3T (24). These errors are relatively small considering that end-systolic myocardial displacement relative to end diastole is of the order of 5 mm. To validate the theoretical analysis, we performed a stationary phantom experiment in the presence of 130 Hz peak-to-peak B_0 variation and calculated the resulting errors in displacement and strain.

EXPERIMENTAL

Pulse sequence

An electrocardiogram (ECG) gated cine displacement-encoded MRI pulse sequence using b-SSFP readouts was implemented on a 3T whole-body MR scanner (MAGNETOM Tim Trio; Siemens Medical Solutions, Erlangen, Germany) equipped with a 12-channel phased array RF coil and a gradient system capable of achieving a maximum gradient strength of 45 mT/m and a slew rate of 200 T/m/s.

The b-SSFP displacement-encoded MRI pulse sequence is similar to the previously described b-SSFP CSPAMM pulse sequence (16) (see Figure 3 in reference 16 for the pulse sequence diagram). Briefly, the magnetization was prepared immediately after the ECG detection at end diastole by interrupting the steady state of magnetization using an '$\alpha/2$' pulse (14–16,25) followed by gradient spoiling, 1-1 SPAMM tagging, and gradient spoiling pulses. Each 90° RF pulse duration was 1 ms, and the second 90° RF pulse was phase cycled between 0 and 180° to acquire CSPAMM data. The displacement-encoding gradient with 0.3 ms pulse duration was applied in the frequency-encoding direction between the two 90° RF pulses, to achieve an encoding strength of 0.94 radians/mm. Spoiler gradients with 1.3 ms pulse duration were applied in both the slice-selective and phase-encoding directions, to achieve a net zeroth gradient moment of 40 mT/m·ms. The total time spent on magnetization preparation (spoil + tagging + spoil) was 4.9 ms for each cardiac cycle. Immediately after magnetization preparation, cine b-SSFP imaging was performed using linearly increasing startup excitation pulse (α) angles (16,26) through the first cardiac phase (12 excitations) and using full excitation angle thereafter, to minimize the signal oscillation caused by the interruption of the steady state of magnetization.

This study implemented two strategies to reduce the off-resonance effects in b-SSFP imaging at 3T. Firstly, the use of low α (see phantom imaging in the Methods section) allowed a reduction in the α pulse duration from 1.2 ms to 0.4 ms. This reduction decreased the *TR* by 0.8 ms. Secondly, a resonance frequency localizer was performed to further reduce the off-resonance effects due to B_0 inhomogeneity and susceptibility.

The b-SSFP imaging parameters included: field of view = 320 × 320 mm; acquisition matrix = 192 (frequency-encoding) × 72 (phase-encoding) per displacement-encoding direction; slice thickness = 7 mm; *TE*/*TR* = 1.47/2.93 ms; number of phase-encoding lines per cardiac phase = 12; temporal resolution = 35 ms; TSENSE acceleration rate (R) = 2; and receiver bandwidth = 745 Hz/pixel.

Two orthogonal multiphase CSPAMM data sets were sequentially acquired. Note that displacement-encoding in the orthogonal direction was achieved by swapping of the frequency-encoding and phase-encoding directions. The acquisition time for each multiphase CSPAMM image set was 12 and 6 heartbeats for the non-accelerated and twofold accelerated b-SSFP acquisitions, respectively. The total acquisition time for acquiring two orthogonal sets of CSPAMM data was 24 and 12 heartbeats for the non-accelerated and twofold accelerated b-SSFP acquisitions, respectively.

Interleaved echo-planar imaging (EPI) (27,28) acquisition was performed to compare its image quality with that produced by the b-SSFP acquisitions. The non-accelerated cine EPI protocol used the same set of imaging parameters, except acquisition matrix = 192 × 54, *TE*/*TR* = 6.15/11.7 ms, echo train length = 3, echo spacing = 2.34 ms, number of phase-encoding lines per cardiac phase = 9, and bottom-up k-space trajectory. The echo-time-shift technique was implemented to reduce the ghosting artifacts caused by off-resonance (29). Flyback readout gradients were used to suppress ghosting artifacts due to B_0 inhomogeneities and motion artifacts (30–32). Although the use of short echo train readout with flyback gradients considerably reduced the image acquisition efficiency compared with the previously used long echo train readout at 1.5T, this strategy was observed to be necessary to suppress motion artifacts and off-resonance effects at 3T. The total acquisition time for acquiring two orthogonal sets of CSPAMM data was 24 heartbeats. Compared with the b-SSFP acquisitions, the cine EPI acquisition has a slightly lower resolution in the phase-encoding direction (b-SSFP acquired 72 k-space lines; cine EPI acquired 54 k-space lines). For comparison at equivalent voxel resolution, the SNR for cine EPI acquisition was scaled by a multiplying factor of 0.75 (or 54/72).

DOI: 10.1002/nbm

Phantom imaging

Phantom experiments were performed to empirically determine the optimal excitation angle (α) for myocardium and to evaluate the effectiveness of the intrinsic phase correction in the echo-combination image reconstruction. The agarose gel phantom had relaxation times ($T_1 \approx 1100$ ms and $T_2 \approx 40$ ms) comparable to those of the myocardium at 3T. Phantom experiments were performed with simulated ECG gating at 60 beats per minute.

To determine the optimal α that achieves relatively high SNR and long tag persistence, the non-accelerated and twofold accelerated b-SSFP acquisitions were repeated with α values ranging from 10° to 30° (10° steps), and cine EPI acquisition was repeated with α values ranging from 10° to 20° (5° steps). The mean SNR of the phantom was calculated. For each α, the SNR was normalized by the maximum SNR value achieved by the middle α (e.g. $\alpha = 20°$ for b-SSFP and $\alpha = 15°$ for EPI) and plotted as a function of time.

To verify the effectiveness of the intrinsic phase correction in the echo-combination reconstruction, the image acquisitions were performed with altered shim currents to emulate the 130 Hz peak-to-peak B_0 variation in the heart at 3T (24). To estimate the measurement errors within the phantom, the root-mean-square (RMS) values were calculated for the magnitude of displacement and strain. To evaluate the agreement between non-accelerated and accelerated b-SSFP acquisitions, Bland–Altman analyses were performed on the magnitude of displacement and strain measurements on a pixel-by-pixel basis.

Cardiac imaging

Six healthy human subjects (three male; three female; minimum/median/maximum age = 24/30/37 years), with no history of heart disease and no risk factors for coronary artery disease, were imaged in three short-axis views (apical, mid-ventricular, basal) of the heart. Non-accelerated and twofold accelerated b-SSFP acquisitions were performed using the optimal α, as determined by the phantom experiment. In three subjects, non-accelerated cine EPI acquisition was also performed using its optimal α for SNR comparison. Human imaging was performed in accordance with protocols approved by the human investigation committee at our institution, and all subjects gave written informed consent.

Image reconstruction and analysis

Image reconstruction and analysis were performed off-line using our image analysis software developed in MATLAB (The Mathworks, Inc., Natick, MA, USA). Figure 2 shows a flow chart diagram that illustrates the overall image reconstruction. For each of two displacement-encoding directions, the CSPAMM k-space data were zero-filled to 192×96. In principle, the CSPAMM subtraction can eliminate the artifact-generating echo due to T1 relaxation. In practice, however, a combination of heart rate variability and motion may cause incomplete subtraction of the artifact-generating echo. To remove the residual artifact-generating signal while minimizing the Gibbs ringing artifacts, an inverted 2D Gaussian filter with the kernel size of 48×48 pixels and the full width at half maximum (FWHM) of 14.8 pixels was applied at the origin of the CSPAMM k-space data. Next, the filtered complex CSPAMM k-space data were divided into two 96×96 k-space matrices, which were separately reconstructed and then combined by the echo-combination reconstruction, as previously described (9). The phase-difference reconstruction was performed using the multiple coil phase-array method, as previously described (33).

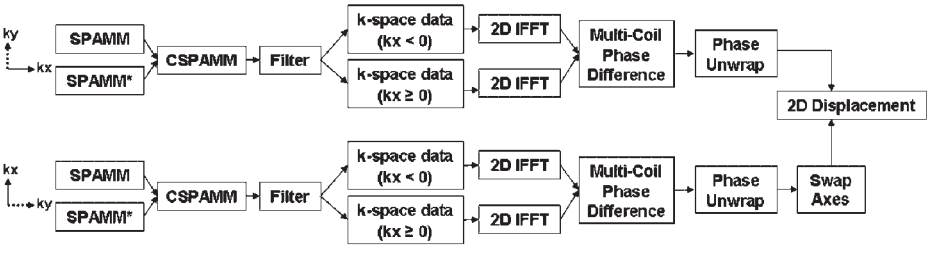

Figure 2. A flow chart diagram illustrating the overall image reconstruction. For each of two displacement- encoding directions, CSPAMM k-space data were subtracted to suppress the artifact-generating echo due to T_1 relaxation. To remove the residual artifact-generating signal while minimizing the Gibbs ringing artifacts, an inverted 2D Gaussian filter with the kernel size of 48×48 pixels and FWHM of 14.8 pixels was applied at the origin of the CSPAMM k-space data. Next, the filtered complex CSPAMM k-space data were divided into two 96×96 k-space matrices, which were separately reconstructed and combined by the echo-combination reconstruction. The phase-difference operation in the echo-combination reconstruction was performed using the multiple-coil phased-array method. After phase unwrapping, the 2D displacement map was calculated as the vector addition of orthogonal 1D displacement values.

DOI: 10.1002/nbm

The resulting FWHM of the point-spread-function in the frequency-encoding direction after the echo-combination reconstruction with filtering was calculated to be 3.6 mm. Hence, the effective spatial resolution of the composite 2D displacement-encoded data was 3.6×3.6 mm. For convenience, the composite data were displayed with a spatial resolution of 3.33×3.33 mm.

TSENSE parallel image reconstruction

The TSENSE parallel image reconstruction (21) was performed to accelerate the cine displacement-encoded MRI acquisition by a factor of 2. The phase encoding order of the multiple heartbeat cine loop was interleaved between successive cardiac phases (i.e. even and odd lines acquired on even and odd phases, respectively). All of the cardiac phases of each cardiac cycle were used to generate a low temporal resolution reference image with full spatial resolution. This image was then used to generate the B_1 field maps and the coil-dependent sensitivity coefficients for the TSENSE reconstruction. SNR-based regularization was used on the basis of the root-sum-of-squares magnitude of the reference image scaled in SNR units (34) based on noise acquired during prescan.

Evaluation of myocardial SNR

The phased-array image reconstruction method was used to reconstruct magnitude images in SNR units, as previously described (34). This reconstruction facilitated accurate and precise SNR measurement on a per pixel basis, without the need to estimate the background noise. Endocardial and epicardial contour segmentation was performed manually. For each displacement-encoding direction, a composite image was reconstructed as the mean of two sub-sampled magnitude images that are produced by the echo-combination image reconstruction. Subsequently, the two orthogonal composite magnitude images were averaged, and the mean myocardial SNR was calculated as the mean intensity within the region of interest defined by the two contours as a function of cardiac phase. The reported SNR represents mean $\pm$ standard deviation across subjects.

Displacement and strain calculations

After the echo-combination reconstruction, a minimum-cost-match algorithm (35) was applied to unwrap the phase within the region of interest defined by the two cardiac contours. Displacement and strain values were calculated as previously described (10). Briefly, 2D displacement was computed by vector addition of two orthogonal one-dimensional (1D) displacement sets. The second principle strain (E_2) was calculated using a quadrilateral finite element model (36). The use of principal directions allowed calculation of strains which are insensitive to geometric irregularities. In short-axis imaging of the heart, the principal direction of E_2 is primarily circumferential. The three short-axis images were divided into 16 left ventricular segments using the American Heart Association standardized segmentation model (37). The relative accuracy of E_2 between non-accelerated and twofold accelerated b-SSFP acquisitions was evaluated using both linear correlation and Bland–Altman analyses.

RESULTS

Phantom imaging

Figure 3 shows plots of normalized SNR as a function of time for b-SSFP and cine EPI acquisitions. For both non-accelerated and twofold accelerated b-SSFP acquisitions, $\alpha = 20^\circ$ yielded the highest overall SNR throughout the cardiac cycle. For cine EPI acquisition, $\alpha = 15^\circ$ yielded the highest overall SNR throughout the cardiac cycle.

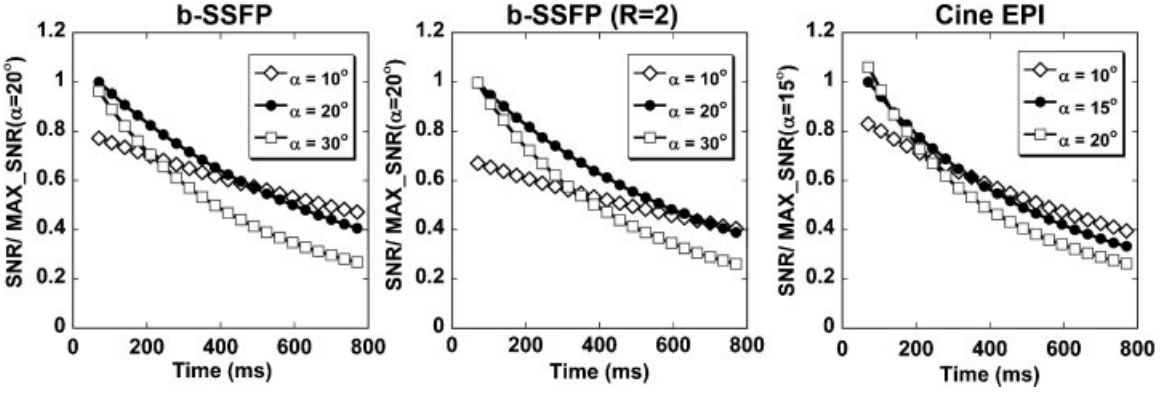

Figure 3. Plots of normalized SNR of the phantom as a function of time for the b-SSFP, b-SSFP with TSENSE, and cine EPI acquisitions. For both non-accelerated and twofold accelerated b-SSFP acquisitions, $\alpha = 20^\circ$ yielded the highest overall SNR throughout the cardiac cycle. For cine EPI acquisition, $\alpha = 15^\circ$ yielded the highest overall SNR throughout the cardiac cycle.

DOI: 10.1002/nbm

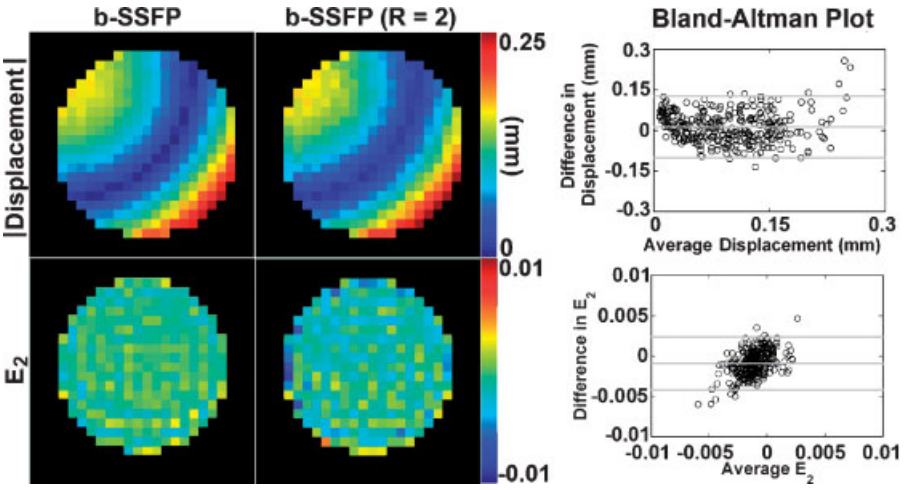

Figure 4. Representative displacement and E_2 error maps of the phantom which illustrate the effectiveness of the intrinsic phase correction in the presence of spatially varying 130 Hz peak-to-peak B_0 variation. In the displacement maps, the systematic error was dominant over the random noise error, as the two acquisitions yielded comparable RMS of displacement (0.11 versus 0.11 mm). In the E_2 maps, both the systematic and random errors contributed comparatively little for both acquisitions. However, the RMS of E_2 was lower for the non-accelerated acquisition than the twofold accelerated acquisition (-0.001 versus -0.002). The error measurements between the non-accelerated and twofold accelerated b-SSFP acquisitions were in good agreement and showed no apparent trend. The gray lines represent the mean $\pm$ 2 standard deviation limits of the Bland–Altman plot.

In Fig. 4, the displacement and E_2 error maps are shown to illustrate the effectiveness of the intrinsic phase correction in the presence of 130 Hz peak-to-peak B_0 variation. In the displacement maps, the systematic error was dominant over the random noise error, as the two acquisitions yielded comparable RMS of displacement (0.11 versus 0.11 mm). In the E_2 maps, both the systematic and random errors contributed comparatively little for both acquisitions. However, the RMS of E_2 was lower for the non-accelerated acquisition than the twofold accelerated acquisition (-0.001 versus -0.002). The error measurements between the non-accelerated and twofold accelerated b-SSFP acquisitions were in good agreement and showed no apparent trend (Fig. 4). Cine EPI data produced geometric distortion at 130 Hz peak-to-peak B_0 variation (data not shown). Therefore, E_2 was not calculated for the cine EPI acquisition.

Cardiac imaging

Figure 5 shows representative magnitude images that compare the image quality between b-SSFP, b-SSFP with TSENSE, and cine EPI acquisitions. The non-accelerated and twofold accelerated b-SSFP acquisitions yielded relatively undistorted images, whereas the cine EPI acquisition produced spatially varying geometric distortion that produced poor image registration of two orthogonal data sets. Therefore, strain analysis was not performed for the cine EPI data.

Figure 6 shows the SNR as a function of time for b-SSFP and cine EPI acquisitions. Compared with the 24-heartbeat cine EPI acquisition, the 24-heartbeat non-accelerated b-SSFP acquisition yielded approximately 65% higher SNR, and the 12-heartbeat twofold accelerated b-SSFP acquisition yielded approximately 28% higher SNR. The twofold accelerated b-SSFP acquisition yielded relatively high SNR (31.2 ± 5.4 at end diastole; 19.9 ± 3.6 at end systole; 10.3 ± 1.1 at late diastole; six subjects; three short-axis views) within a clinically feasible breath-hold duration of 12 heartbeats.

In Fig. 7, a representative set of non-accelerated and twofold accelerated b-SSFP functional data from the same subject at end systole is shown to illustrate the reproducibility between the two acquisitions. Statistically, E_2 values measured by the non-accelerated and twofold accelerated acquisitions correlated strongly (slope $= 0.99$; bias $= -0.00$; $R^2 = 0.91$), and the measurements were in excellent agreement, with a mean difference of 0.00, and showed no apparent trend (Fig. 8). Together with the SNR results, these data demonstrate that the combined use of b-SSFP imaging and 3T acquisition can yield sufficient SNR to tolerate the accompanying SNR loss due to a twofold undersampling.

In Fig. 9, representative functional maps acquired using the twofold accelerated protocol are shown in three short-axis levels of the heart. The combined use of short α pulses and resonance frequency localizer effectively minimized the off-resonance effects for all 18 short-axis views imaged in this study.

DOI: 10.1002/nbm

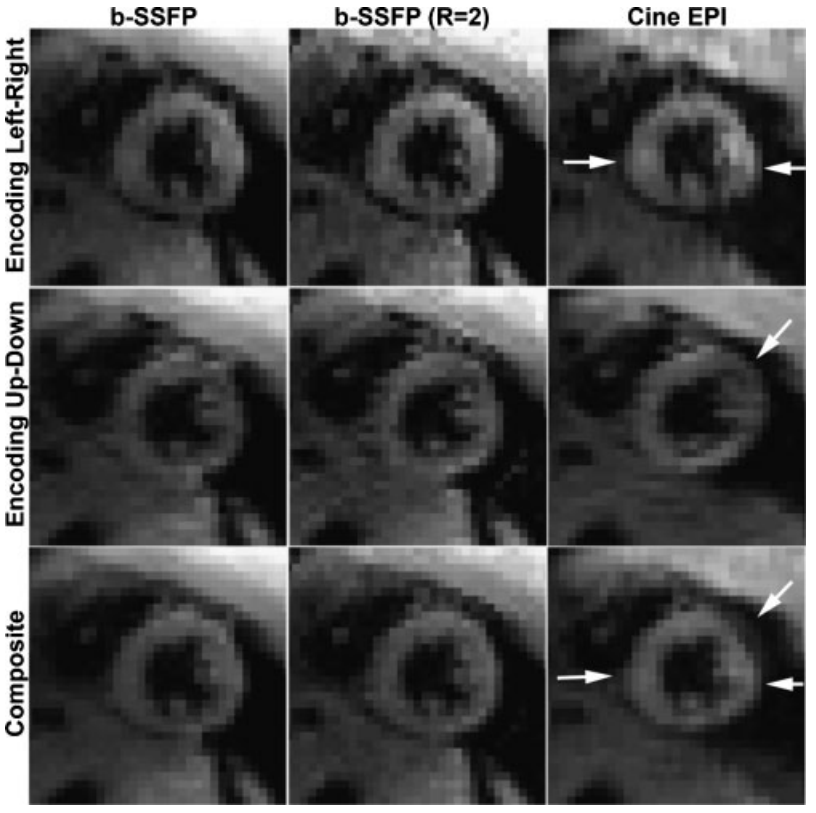

Figure 5. Representative magnitude images that compare the image quality between the b-SSFP, b-SSFP with TSENSE, and cine EPI acquisitions. The non-accelerated and twofold accelerated b-SSFP acquisitions yielded relatively undistorted images, whereas the cine EPI acquisition produced spatially varying geometric distortion that produced poor image registration of two orthogonal data sets. Arrows point to a distorted region of the myocardium.

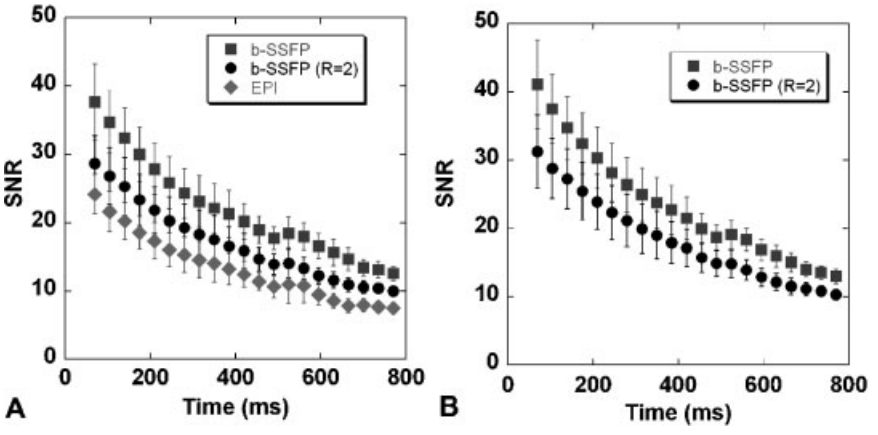

Figure 6. (A) Plots of mean myocardial SNR as a function of time for the b-SSFP, b-SSFP with TSENSE, and cine EPI acquisitions ($n = 3$). Compared with the cine EPI acquisition, the non-accelerated b-SSFP acquisition yielded approximately 65% higher SNR, and the twofold accelerated b-SSFP acquisition yielded approximately 28% higher SNR. (B) The twofold accelerated b-SSFP acquisition yielded relatively high SNR ($n = 6$; 31.2 ± 5.4 at end diastole; 19.9 ± 3.6 at end systole; 10.3 ± 1.1 at late diastole) within a clinically feasible breath-hold duration of 12 heartbeats. These results demonstrate that a combined use of b-SSFP imaging and 3T acquisition can yield sufficient SNR to tolerate the accompanying SNR loss due to a twofold undersampling.

DOI: 10.1002/nbm

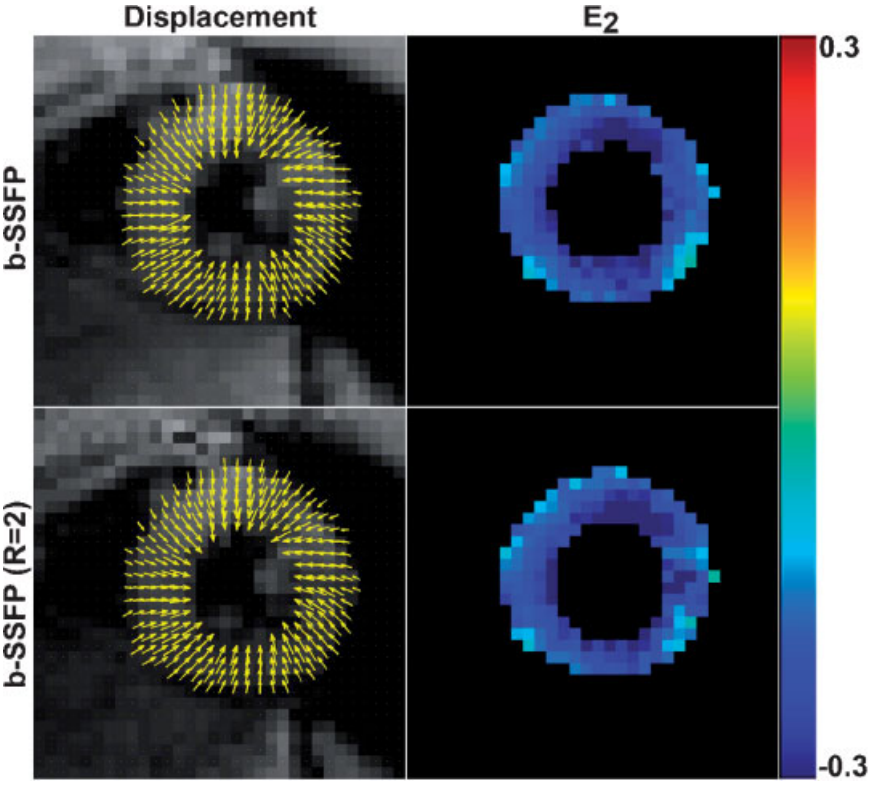

Figure 7. Representative functional data sets comparing the image quality between the non-accelerated (top row) and twofold accelerated (bottom row) b-SSFP acquisitions: magnitude image superimposed with 2D vector displacement map (left column) and E_2 map (right column). The two image sets representing the same subject, cardiac phase, and short-axis plane appear very similar.

DISCUSSION

This study demonstrates that a combined implementation of b-SSFP imaging, 3T imaging, and TSENSE parallel imaging can be used to improve the SNR and data acquisition efficiency of cine displacement-encoded MRI. In a limited number of subjects, the 12-heartbeat b-SSFP acquisition with TSENSE yielded approximately 28% higher SNR than the 24-heartbeat cine EPI acquisition. This 12-heartbeat cine displacement-encoded MRI sequence can yield 2D functional maps with nominal spatial resolution of 3.6×3.6 mm (including image blurring due to filtering), temporal resolution of 35 ms, and relatively high SNR.

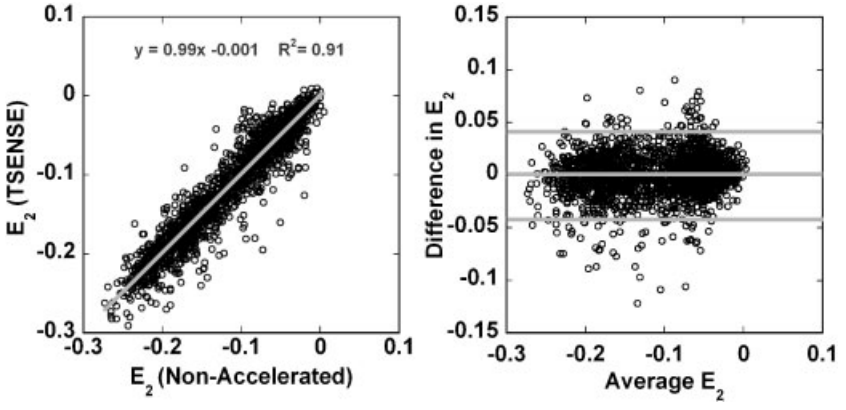

Figure 8. Scatter plots showing linear correlation (left) and Bland–Altman (right) analyses on E_2 measurements between the non-accelerated and twofold accelerated acquisitions. The E_2 measurements correlated strongly (slope = 0.98; bias = −0.00; $R^2 = 0.91$) and were in excellent agreement, with a mean difference of 0.00. The gray lines represent the fitted slope of the linear correlation plot, as well as the mean ± 2 standard deviation limits of the Bland–Altman plot.

DOI: 10.1002/nbm

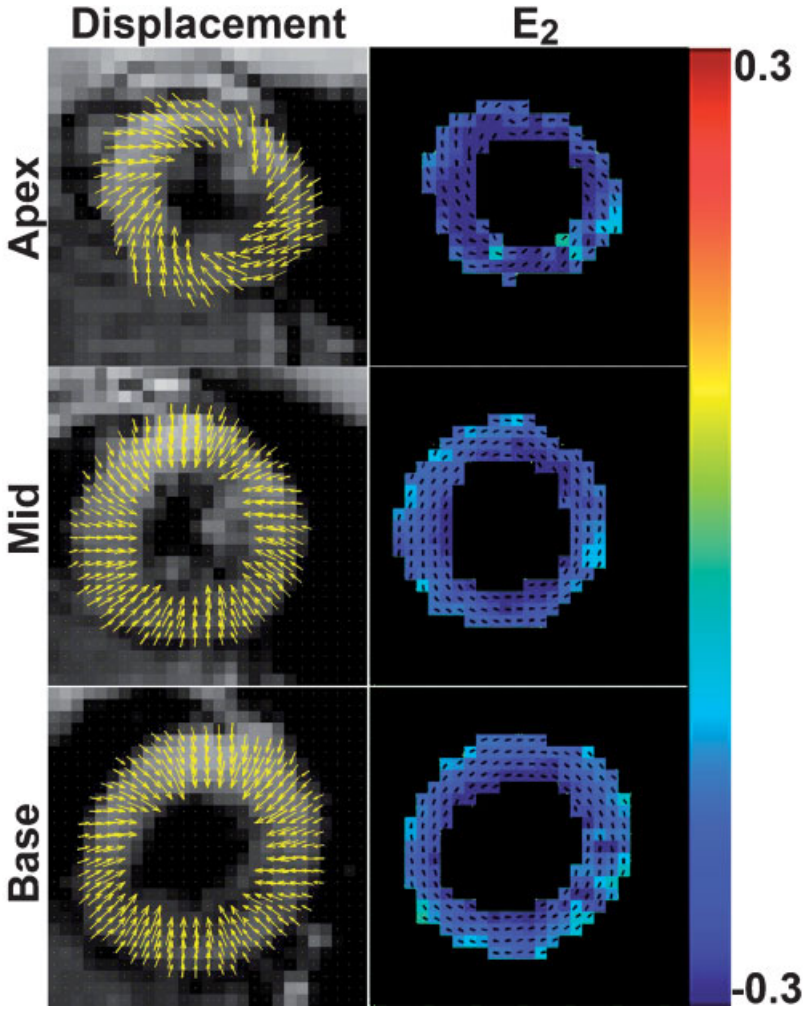

Figure 9. Representative functional maps acquired using the twofold accelerated protocol are shown in three short-axis levels of the heart. The combined use of short α pulses and resonance frequency localizer effectively minimized the off-resonance effects for all 18 short-axis views imaged in this study.

Displacement-encoded MRI has been previously implemented with SENSE (20) for a single cardiac phase application that acquired a low spatial resolution reference image for coil sensitivity maps. The proposed method incorporates parallel imaging in cine displacement-encoded MRI using auto-calibrated TSENSE reconstruction.

The error analysis of the phantom results suggests that the intrinsic phase correction in the echo-combination reconstruction can effectively reduce the residual phase error due to 130 Hz peak-to-peak B_0 variation for accurate strain analysis. In the displacement calculation, the systematic phase error was dominant over the random noise error for both the non-accelerated and twofold accelerated acquisitions, probably owing to the relatively high SNR produced by both protocols. This balance of error contribution to displacement may not be valid for acquisitions with poor SNR. The displacement error of 0.11 mm is relatively small. One approach to further reduce the displacement error is to increase the receiver bandwidth (i.e. shorten the time interval between the echoes) at the expense of lower SNR. A second approach is to perform more effective shimming. In the E_2 calculation, both the systematic and random phase errors contributed comparatively little for both acquisitions. However, the RMS of E_2 was lower for the non-accelerated acquisition than the twofold accelerated acquisition (-0.001 versus -0.002). Again, this balance of error contribution to E_2 may not be valid for acquisitions with poor SNR. The observed finding is consistent with the fact that strain is more sensitive to noise than displacement. The Bland–Altman analysis of *in vivo* E_2 measurements suggests that the systematic error contribution was negligible and that the SNR was sufficiently high to swamp the random noise error. Future work will include a more comprehensive analysis by

DOI: 10.1002/nbm

evaluating the effects of SNR, B_0 variation, and motion on the systematic and random errors in displacement and strain calculations.

Technical challenges of b-SSFP imaging at 3T include dark band artifacts due to B_0 inhomogeneities and susceptibility and specific absorption rate limit. In this work, the α pulse duration was reduced from 1.2 ms to 0.4 ms in order to reduce the *TR* by 0.8 ms, and a resonance frequency localizer was performed to further reduce the off-resonance effects. The use of small excitations ($\alpha = 20^\circ$) did not exceed the limit of the specific absorption rate at 3T.

Despite the interesting findings, this study has several limitations. Firstly, the residual phase error may yield small displacement errors as already discussed. Secondly, the use of linearly increasing startup excitation angles produced non-diagnostic image quality for the first cardiac phase. However, this is not a practical problem because the strain at the first cardiac phase can be assumed to be zero. Thirdly, this study did not include patients with limited breath-hold capacity and heart rate irregularities, which may degrade the overall image quality. However, the image degradation due to these irregularities may be minimized by decreasing the acquisition time using TSENSE. Fourthly, this study did not include the performance of cine displacement-encoded MRI using gradient echo imaging because of its low data acquisition efficiency. Fifthly, this study was performed using manual contour segmentation at approximately 15–20 min per 2D slice of 18–22 cardiac phases. This limitation needs to be addressed in order to make cine displacement-encoded MRI practical for routine clinical use. Future work will include implementation of semi-automated segmentation algorithms that are comparable in accuracy to manual segmentation.

Acknowledgements

We thank Vinay Pai, Ph.D., for helpful insights into b-SSFP acquisition, and KellyAnn McGorty, B.S.R.T., for assistance with MR scanning.

REFERENCES

1. Sutherland GR, Stewart MJ, Groundstroem KW, Moran CM, Fleming A, Guell-Peris FJ, Riemersma RA, Fenn LN, Fox KA, McDicken WN. Color Doppler myocardial imaging: a new technique for the assessment of myocardial function. *J. Am. Soc. Echocardiogr.* 1994; **7**: 441–458.
2. Axel L, Dougherty L. MR imaging of motion with spatial modulation of magnetization. *Radiology* 1989; **171**: 841–845.
3. Zerhouni EA, Parish DM, Rogers WJ, Yang A, Shapiro EP. Human heart: tagging with MR imaging: a method for noninvasive assessment of myocardial motion. *Radiology* 1988; **169**: 59–63.
4. Pelc LR, Sayre J, Yun K, Castro LJ, Herfkens RJ, Miller DC, Pelc NJ. Evaluation of myocardial motion tracking with cine-phase contrast magnetic resonance imaging. *Invest. Radiol.* 1994; **29**: 1038–1042.
5. van Dijk P. Direct cardiac NMR imaging of heart wall and blood flow velocity. *J. Comput. Assist. Tomogr.* 1984; **8**: 429–436.
6. Wedeen VJ. Magnetic resonance imaging of myocardial kinematics. Technique to detect, localize, and quantify the strain rates of the active human myocardium. *Magn. Reson. Med.* 1992; **27**: 52–67.
7. Osman NF, Kerwin WS, McVeigh ER, Prince JL. Cardiac motion tracking using CINE harmonic phase (HARP) magnetic resonance imaging. *Magn. Reson. Med.* 1999; **42**: 1048–1060.
8. Aletras AH, Ding S, Balaban RS, Wen H. DENSE: displacement encoding with stimulated echoes in cardiac functional MRI. *J. Magn. Reson.* 1999: 247–252.
9. Kim D, Epstein FH, Gilson WD, Axel L. Increasing the signal-to-noise ratio in DENSE MRI by combining displacement-encoded echoes. *Magn. Reson. Med.* 2004; **52**: 188–192.
10. Kim D, Gilson WD, Kramer CM, Epstein FH. Myocardial tissue tracking with two-dimensional cine displacement-encoded MR imaging: development and initial evaluation. *Radiology* 2004; **230**: 862–871.
11. Ryf S, Tsao J, Schwitter J, Stuessi A, Boesiger P. Peak-combination HARP: a method to correct for phase errors in HARP. *J. Magn. Reson. Imaging.* 2004; **20**: 874–880.
12. Carr H. Steady-state free precession in nuclear magnetic resonance. *Phys. Rev.* 1958; **112**: 1693–1701.
13. Oppelt A, Graumann R, Barfuss H, Fischer H, Hartl W, Schajor W. FISP: a new fast MRI sequence. *Electromedica* 1986; **54**: 15–18.
14. Herzka DA, Guttman MA, McVeigh ER. Myocardial tagging with SSFP. *Magn. Reson. Med.* 2003; **49**: 329–340.
15. Markl M, Reeder SB, Chan FP, Alley MT, Herfkens RJ, Pelc NJ. Steady-state free precession MR imaging: improved myocardial tag persistence and signal-to-noise ratio for analysis of myocardial motion. *Radiology* 2004; **230**: 852–861.
16. Zwanenburg JJ, Kuijer JP, Marcus JT, Heethaar RM. Steady-state free precession with myocardial tagging: CSPAMM in a single breathhold [erratum appears in Magn. Reson. Med. 2003; 50: 228]. *Magn. Reson. Med.* 2003; **49**: 722–730.
17. Bennett EE, Pai VM, Wen H. Ultrafast DENSE technique for mapping the volumetric 3D wall motion of the left ventricle. In: Proceedings of 10 th Annual Meeting ISMRM, Honolulu, USA. 2002. p 775.
18. Epstein FH, Voros S, Gilson WD, Kramer CM. Quantitative wall motion imaging by cine DENSE in acute myocardial infarction: initial experience using an SSFP-based sequence. In: Proceedings of 6th Annual Meeting SCMR, Barcelona, Spain, 2004; abstract 490.
19. Pruessmann KP, Weiger M, Scheidegger MB, Boesiger P. SENSE: sensitivity encoding for fast MRI. *Magn. Reson. Med.* 1999: 952–962.
20. Aletras AH, Ingkanisorn WP, Mancini C, Arai AE. DENSE with SENSE. *J. Magn. Reson.* 2005; **176**(1): 99–106.
21. Kellman P, Epstein FH, McVeigh ER. Adaptive sensitivity encoding incorporating temporal filtering (TSENSE). *Magn. Reson. Med.* 2001; **45**: 846–852.
22. Fischer SE, McKinnon GC, Maier SE, Boesiger P. Improved myocardial tagging contrast. *Magn. Reson. Med.* 1993; **30**: 191–200.
23. Kuijer JP, Jansen E, Marcus JT, van Rossum AC, Heethaar RM. Improved harmonic phase myocardial strain maps. *Magn. Reson. Med.* 2001; **46**: 993–999.
24. Noeske R, Seifert F, Rhein KH, Rinneberg H. Human cardiac imaging at 3 T using phased array coils. *Magn. Reson. Med.* 2000; **44**: 978–982.
25. Scheffler K, Heid O, Hennig J. Magnetization preparation during the steady state: fat-saturated 3D TrueFISP. *Magn. Reson. Med.* 2001; **45**: 1075–1080.
26. Deshpande VS, Shea SM, Laub G, Simonetti OP, Finn JP, Li D. 3D magnetization-prepared true-FISP: a new technique for imaging coronary arteries. *Magn. Reson. Med.* 2001; **46**: 494–502.
27. Epstein FH, Wolff SD, Arai AE. Segmented k-space fast cardiac imaging using an echo-train readout. *Magn. Reson. Med.* 1999; **41**: 609–613.
28. Reeder SB, Atalar E, Faranesh AZ, McVeigh ER. Multi-echo segmented k-space imaging: an optimized hybrid sequence

DOI: 10.1002/nbm

for ultrafast cardiac imaging. *Magn. Reson. Med.* 1999; **41**: 375–385.
29. Feinberg DA, Oshio K. Gradient-echo shifting in fast MRI techniques (GRASE imaging) for correction of field inhomogeneity errors and chemical shift. *J. Magn. Reson.* 1992; **97**: 177–183.
30. Feinberg DA, Turner R, Jakab PD, von Kienlin M. Echo-planar imaging with asymmetric gradient modulation and inner-volume excitation. *Magn. Reson. Med.* 1990: 162–169.
31. Duerk JL, Simonetti OP. Theoretical aspects of motion sensitivity and compensation in echo-planar imaging. *J. Magn. Reson. Imaging.* 1991: 643–650.
32. Kim D, Bove CM, Kramer CM, Epstein FH. Importance of k-space trajectory in echo-planar myocardial tagging at rest and during dobutamine stress. *Magn. Reson. Med.* 2003; **50**: 813–820.
33. Bernstein MA, Grgic M, Brosnan TJ, Pelc NJ. Reconstructions of phase contrast, phased array multicoil data. *Magn. Reson. Med.* 1994: 330–334.
34. Kellman P, McVeigh ER. Image reconstruction in SNR units: a general method for SNR measurement. *Magn. Reson. Med.* 2005; **54**: 1439–1447.
35. Buckland JR, Huntley JM, Turner SRE. Unwrapping noisy phase maps by use of a minimum-cost-matching algorithm. *Appl. Opt.* 1995; **34**: 5100–5108.
36. Moaveni S. *Finite element analysis: theory and application with ANSYS*. Prentice Hall: Upper Saddle River, NJ, 1999.
37. Cerqueira MD, Weissman NJ, Dilsizian V, Jacobs AK, Kaul S, Laskey WK, Pennell DJ, Rumberger JA, Ryan T, Verani MS, American Heart Association Writing Group on Myocardial S, Registration for Cardiac I. Standardized myocardial segmentation and nomenclature for tomographic imaging of the heart: a statement for healthcare professionals from the Cardiac Imaging Committee of the Council on Clinical Cardiology of the American Heart Association. *Circulation* 2002; **105**: 539–542.

DOI: 10.1002/nbm